

www.acsaem.org Article

Optimization of the Li₃BO₃ Glass Interlayer for Garnet-Based All-Solid-State Lithium—Metal Batteries

Zhenghuan Tang, Junbin Choi, Jose L. Lorie Lopez, Anne C. Co, Christopher J. Brooks, Jay R. Sayre,* and Jung-Hyun Kim*



Cite This: ACS Appl. Energy Mater. 2022, 5, 12132-12142



ACCESS I

III Metrics & More

Article Recommendations

SI Supporting Information

ABSTRACT: Lithium (Li)-dendrite penetration and poor interfacial wetting between Li-metal anode and the solid electrolyte are two major potential drawbacks concerning the long-term performance of garnet-based solid-state Li-metal batteries (SSLBs). To address these problems, the amorphous Li_3BO_3 (LBO) glass interlayer in between Li anode and the solid electrolyte was demonstrated as a promising solution. However, this approach requires a thorough optimization to achieve effective performance and safety improvements in SSLBs. In this work, systematic design of experiments revealed optimal synthesis parameters stepwise to obtain a thin and uniform LBO interlayer in between $\text{Li}_{6.4}\text{La}_3\text{Zr}_{1.6}\text{Ta}_{0.6}\text{O}_{12}$ (LLZT) solid electrolyte and Li anode by using a screen-printing technique. The investigated synthesis



parameters included LBO slurry compositions, heating rates, heating temperatures, heating times, and cooling rates. As a result, a pinhole-free LBO glass layer with ~5 μ m thickness could be coated onto LLZT pellets. The resulting LBO interlayer enhanced Limetal wetting and increased the interfacial conductivity from 1.32 × 10⁻⁴ (from LBO-free) to 1.06 × 10⁻³ S/cm. Electrochemical characterization of symmetrical cells revealed positive roles of the LBO interlayer such as (i) reducing interfacial impedance and offering uniform current flow across interfaces, (ii) preventing Li-dendrite penetration, and (iii) increasing the critical current density (CCD) and cycle life of SSLBs.

KEYWORDS: glass interlayer, Li₃BO₃, garnet solid electrolyte, Li dendrite, solid-state batteries

INTRODUCTION

Recently, all-solid-state Li-metal batteries (SSLBs) have received increasing attention as the next-generation energy storage devices due to the high energy density, potential for enhanced safety, and thermal stability. Among various types of solid electrolytes (SEs) such as Li-stuffed garnet-phase oxides,² perovskite,³ NASICON,⁴ lithium phosphorus oxynitride (LiPON),⁵ and anti-perovskite,⁶ garnet-type Li₇La₃Zr₂O₁₂ (LLZO) delivered a high ionic conductivity ($\sim 10^{-4}$ S/cm) and a wide electrochemical stability window. 7,8 The chemical compositions of the LLZO-based garnet phases have been tailored by substituting Ga, Si, In, Ge, and Ta for Zr in LLZO to improve the performance while stabilizing the crystal phase.9 For example, El Shinawi et al. 10 demonstrated a stabilization of the LLZO crystal phase by Ga substitution. Huang et al.¹¹ reported that Ge substitution for Zr in LLZO enhanced the ionic conductivity to 7.63×10^{-4} S/cm, while Si and In substitutions adversely effected the conductivity values. Allen et al. 12 reported 8.7×10^{-4} S/cm conductivity from Tasubstituted LLZO (e.g., Li_{6.75}La₃Zr_{1.75}Ta_{0.25}O₁₂). Further optimization of the Ta substitution could achieve an even higher ionic conductivity value of 1.0×10^{-3} S/cm from $Li_{6.4}La_3Zr_{1.6}Ta_{0.6}O_{12}$ (LLZT).¹³

Despite the promising ionic conductivity, there are a few technical challenges that prevent the implementation of LLZT in practical SSLBs. First, LLZT suffers from a high interfacial resistance due to the poor wetting observed at the Li/SE interfaces, as evidenced by their large contact angle of 146°. 14 Such a lithiophobic property of LLZT makes Li deposition challenging. Second, LLZT suffers from Li-dendrite penetration through grain boundaries and local pre-existing cracks during cycling.¹⁵ Due to the high electrical and low ionic conductivities at grain boundaries, Li ions and electrons are attracted to form metallic Li along grain boundaries. 16,17 In addition, poor wetting at the Li/SE interface could limit a contact between Li anode and LLZT. Therefore, electrical current could be concentrated on those limited interfacial areas and unwantedly accelerated the Li nucleation and promoted its dendritic growth. 18,19

Received: May 25, 2022 Accepted: September 14, 2022 Published: September 30, 2022





Table 1. Summary of Li⁺-Conducting Glass Material Candidates and Their Properties Reported in the Literature ^{a38–42}

Materials	σ _{Li} (S/cm)	Stability with Li	Melting Temp. (T _m) (°C)	Stability with LLZT at High-Temp.	Synthesis Conditions	Reference
Li₃OCI	2.24×10 ⁻⁴	Poor	282	Not reported	240°C for 6 h in Ar	23
Li₂O	~10-9	Good	1438	Not reported	In-situ reaction @ 200°C	21
LiCI	1.4×10-4	Good	610	Not reported	SEI after cycle	23
Li ₃ PO ₄	3×10 ⁻⁷	Poor	837	Good	1140°C for 16 h in air	21
Li ₃ P	~10-4	Good	650	Good	400°C for 4 h in Ar	21
Li ₃ BO ₃	2×10-6	Good	665	Good	700°C for 5 h and then 900°C for 36 h in air	29
Li ₂ SiO ₃	~10-8	Good	1201	Not reported	350°C for 0.5 h	22
Li ₂ PO ₂ N	8.8×10 ⁻⁷ @80°C	Good	Not reported	Good	950°C for 10 h in vacuum	38,39
LiNbO ₃	~10-6	Good	1257	Good	Not reported	40
9Li ₃ BO ₃ -1Li ₂ SO ₄	~10-5	Not reported	< 900	Not reported	290°C for 1 h	31
Li ₃ PO ₄ -Li ₃ BO ₃ -Li ₂ SO ₄ (25:14:61)	4.9×10 ⁻⁴ @300°C	Good	Li ₃ PO ₄ :837 Li ₃ BO ₃ :1201 Li ₂ SO ₄ :859	Not reported	Not reported	41
Li ₂ O-B ₂ O ₃ -SiO ₂ (65:27:8)	3.6×10-6	Good	Li ₂ O:1438 B ₂ O ₃ :450 SiO ₂ :1726	Not reported	1150°C for 1 h in air	42
Li₃PO₄−Lil−LiCl (50:25:25)	8×10 ⁻⁴	Not reported	Li₃PO₄:837 Lil:469 LiCl: 610	Not reported	Not reported	43

^aGreen color code for desired properties: $\sigma_{\rm Li}$ > 10⁻⁴ S/cm, $T_{\rm m}$ < 700 °C. Yellow color code for acceptable properties: 10⁻⁴ > $\sigma_{\rm Li}$ > 10⁻⁷ S/cm, 700 °C < $T_{\rm m}$ < 1000 °C. Red color code for undesired properties: $\sigma_{\rm Li}$ < 10⁻⁷ S/cm, $T_{\rm m}$ > 1000 °C.

To address the issues, various strategies have been proposed, such as carbon reaction treatment, 20 elemental doping, 10 in situ solid—electrolyte interface (SEI) formation, 21 and designing and engineering interlayers. 15 Among these strategies, interlayer engineering between Li anode and LLZT showed promising advantages of simple processing and manufacturing friendliness. Various interlayer materials such as Li₂SiO₃, 22 Li₃OCl, 23 Li₃PO₄, 21 65 Li₂O–27 B₂O₃–8 SiO₂, 24 and indium tin oxide (ITO) 14 showed enhanced interfacial properties and improved cell performances.

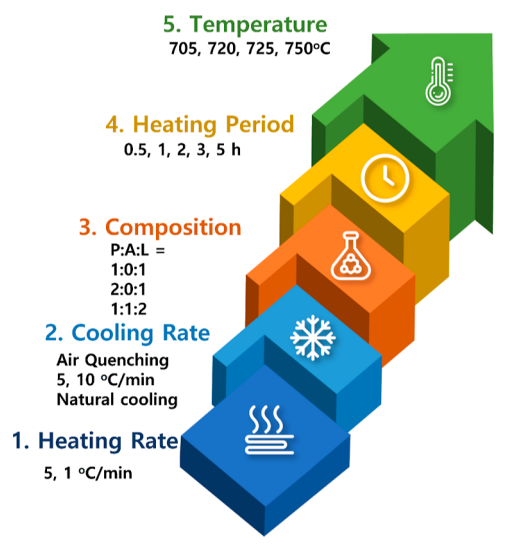
In this work, we focused on amorphous glass interlayers for SSLBs because of their dense and grain-boundary-free structures. Preparation of the amorphous glass layer coating onto the LLZT SE pellet involves melting the glass powders by heating above its melting temperature, followed by cooling. Therefore, a moderate melting temperature of glass (e.g., <800 °C) will be an important criterion to make the manufacturing process easier and avoid a potential risk of unwanted chemical reactions in contact with LLZT. For example, ITO and Li₂SiO₃ will not be suitable for the glass melting process because of their high melting temperatures (e.g., ~1900²⁵ and 1200 °C, ²⁶ respectively). Reasonably good Li-ion conductivity is another important criterion in selecting an amorphous glass interlayer material. For example, the Li₂SiO₃ interlayer could enhance wetting of Li anode onto a solid electrolyte, 22 but its low Li-ion conductivity ($\sim 10^{-8}$ S/cm) could increase the overall cell

resistance.²⁷ In addition, the interlayer needs to be chemically stable in contact with Li metal anodes. Both Li₃OCl²³ and Li₃PO₄²¹ were purposed as excellent interlayer materials with high ionic conductivities (Li₃OCl: 2×10^{-4} S/cm, ²³ Li₃PO₄: $\sim 10^{-5}$ S/cm²⁸) and low heat-treating temperatures (Li₃OCl: 282 °C, ²³ Li₃PO₄: 837 °C²¹). However, both Li₃OCl and Li₃PO₄ can react with Li during cycling and produce Li₂O layers which can degrade the overall conductivity. Furthermore, materials such as Li₃OCl are difficult to synthesize and handle due to their extreme moisture sensitivity. Among those glass material candidates, Li₃BO₃ (LBO) stands out because of its relatively low melting temperature (665 °C), 29 moderate ionic conductivity ($\sim 10^{-6}$ S/cm), 30 good stability in contact with Li metal and LLZT, 31 and facile synthesis process. It was reported that the Li₂CO₃ layer could be found at the LLZT surface and grain boundaries by its moisture contamination. 20,32 Applying the LBO layer and heat-treating the LBOcoated LLZT above 650 °C afterward may absorb some of the Li₂CO₃ at the LLZT pellet surface to form Li_{2.3}C_{0.7}B_{0.3}O₃ (LCBO), which delivers a moderate ionic conductivity (10⁻⁶ to 10^{-7} S/cm). 33,34 Table 1 overviews the key properties of various glass interlayers which have been previously reported in the literature.

Recently, LBO has been examined as a promising interlayer material between Li metal and LLZT.³⁵ In an earlier report, however, LBO was coated onto LLZT pellets by dip coating

using an aqueous solution. Although cell performance and interfacial wetting were improved, dip coating using an aqueous solution still poses potential damages to the LLZT pellets because LLZT is sensitive to moisture. 36 In fact, LiOH formed on the surface and grain boundaries of LLZT pellets when LLZT was in contact with moisture in air, even not with water, significantly perturbing Li-ion conductivity.³⁷ In addition, understanding and optimizing the processing conditions to achieve a homogeneous and dense LBO interlayer are critical for the fabrication of high-quality SSLBs. In this regard, we performed a systematic experimental design to investigate the effect of process conditions on the physical and electrochemical properties of LBO interlayers. Here, the LBO coating slurry was made with a moisture-free solvent, followed by applying onto LLZT pellets by a screenprinting method. Through systematic design of experiments as illustrated in Scheme 1, the effect of synthesis parameters on

Scheme 1. Step-by-step Flow Chart Indicating Each Step of the Optimization Process^a



"During each step, only one parameter was varied, and the rest four parameters were fixed. Here, P/A/L indicates the weight ratio of binder paste, α -terpineol, and LBO powder.

the properties of the LBO interlayer will be discussed. In addition, positive roles of the resulting LBO interlayer to enhance the Li-metal wetting and prevent the Li-dendrite penetration during SSLB cycling will be presented.

■ EXPERIMENTAL SECTION

Synthesis of LLZT and LBO. For the synthesis of LLZT, appropriate amounts of Li_2CO_3 (Alfa Aesar), Ta_2O_5 (Alfa Aesar), ZrO_2 (Alfa Aesar), and La_2O_3 (Acros Organics) were thoroughly mixed in a zirconia ball milling jar with isopropanol as a solvent. The precursors were stirred and ground on a roller mill for 24 h. The solvent, then, was dried overnight, and the remaining powder was calcined at 900 °C for 12 h. The resulting as-prepared powder was stirred and ground again on the roller mill with zirconia balls and isopropanol for 24 h. Finally, after the solvent was removed, the powder was pelletized in a mechanical press, followed by calcination at 1170 °C for 12 h. For the synthesis of LBO, H_3BO_3 (Alfa Aesar) and LiOH (Alfa Aesar) were first added into distilled water in a 1:3 molar ratio and stirred vigorously at 50 °C to make a homogeneous solution. The solution was then dried at 120 °C and stirred under low rpm. The resulting powder was finally heat-treated at 600 °C for 12 h.

Screen Printing of the LBO Coating Layer. Synthesized LBO powder was grounded using a high-energy ball mill (Spexmill) to obtain a fine powder. Before optimization, LBO powder and binder paste (Heraeus) were added into a mortar and pestle in a 1:1 weight ratio and mixed to make a slurry. The resulting LBO slurry was screen-printed onto the LLZT pellet using a 9 mm diameter circle pattern on a #200 mesh board. Three layers were coated onto the pellet, and each fresh layer coated before the previous layer was dried at 80 °C. The coated samples were placed in an Al_2O_3 crucible and heat-treated according to the conditions during optimization steps.

Electrochemical Cell Fabrication. Li foil was first brushed and then punched out with a 5/16 inch diameter punch. The brushed Li foil was first attached to both sides of the LLZT and LBO-LLZT pellets, and pellets with Li foil on both sides were then sandwiched with Cu foils and heated on a hot plate at 220 °C for 3 min. After heat treatment on both sides, the pellet was sealed in a Swagelok-type cell. All the processes were completed in an Ar-filled glovebox.

Sample Characterization. Scanning electron microscopy (SEM, Hitachi S-3000H) images were obtained with an acceleration voltage of 15 kV. Electrochemical impedance spectroscopy (EIS, Gamry 1010E) of selected cells was obtained in a frequency range of 5 MHz to 1 Hz. The critical current density (CCD) value of each assembled Swagelok-type cell was obtained by galvanostatic cyclic measurements starting from 0.05 mA/cm² with a step increase of 0.05 mA/cm². Each step had a 30 min charging event, a 30 min discharging event, and 5 min rest in each of the events. The cell was cycled (i.e., continuous stripping and plating) at a current density of 0.1 mA/cm² with the capacity limit of 0.05 mA h/cm² at 25 °C.

■ RESULTS AND DISCUSSION

In this work, we performed a systematic design of experiments to investigate physical properties of the LBO glass interlayer coated onto the LLZT solid electrolyte. Before optimization, LBO slurry in a weight composition of binder paste/ α terpineol/LBO (P/A/L) = 1:0:1 was coated three times onto LLZT pellets, heated at a rate of 5 °C/min to 750 °C, and dwelled for 5 h, followed by air quenching at room temperature. Referring to Scheme 1, the five-step optimization had five critical parameters, and each of the parameters was altered one by one. Beginning from changing the heating rate, the process was then optimized by tuning the cooling rate, slurry composition, heating time, and heating temperature one by one. After each step, the optimized parameter was carried to the next step. There were two exceptions in the process. First, the heating temperature of 725 °C heating was adopted after the heating rate was optimized as we found that 725 °C was high enough to melt all the LBO layer in 5 h. The other exception was in the process of slurry optimization (step 3). Although natural cooling was selected as the result of the cooling rate optimization, we found the need to optimize slurry composition under harsher conditions, and therefore, roomtemperature quenching was still applied during the slurry optimization.

Effect of Heating Rate on LBO Interlayer Coating. In this section, we report the effect of heating rate on the LBO interlayer on the LLZT pellet. The LBO screen-printed samples were heated to 750 °C at different heating rates of 1 and 5 °C/min. After heating at 750 °C for 5 h, samples were quickly taken out from the furnace and air-quenched to room temperature. Figure 1 shows top-down SEM images comparing the microstructure of the resulting LBO layers from each sample. Because of the back-scattered effect, domains with a darker color correspond to the LBO coating layer due to its lower mean atomic numbers than LLZT. The sample heated at 5 °C/min (Figure 1a) revealed mostly bare LLZT surfaces

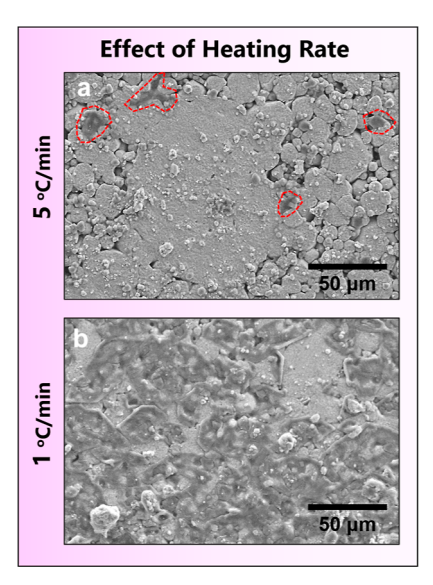


Figure 1. SEM images revealing a surface of the LBO interlayer coated onto LLZT substrate when the heating rates were (a) 5 and (b) 1 $^{\circ}$ C/min. Control variables: slurry composition of P/A/L = 1:0:1, heating at 750 $^{\circ}$ C for 5 h, and air quenching.

with small LBO grains scarcely scattered on the surface. In contrast, Figure 1b shows a better-established coating of the LBO layer obtained from the 1 °C/min heating rate. During the heating process, the organic binder in the binder paste decomposes first at a lower temperature than the LBO melting temperature (e.g., 665 °C). Therefore, binder decomposition during the abrupt heating at the rate of 5 °C/min would disturb uniform LBO particle layer deposition on LLZT and caused the delamination. This result clearly demonstrated that achieving a good-quality LBO interlayer strongly depended on the slow heating rate. Therefore, we adopted the 1 °C/min heating rate during the rest of this work.

Effect of Cooling Rate on LBO Interlayer Coating. As the next step, we investigated the effect of cooling methods. First, we examined two different conditions: (i) air quenching to room temperature and (ii) cooling at 5 °C/min under controlled variables as described in Figure 2. Figure 2 shows top-down SEM images comparing the microstructure of coated layers obtained from these two cooling conditions. The sample cooled by air quenching showed smoother coating which covered most of the LLZT grains. However, there were some micro-sized pinholes which are marked (circled in red) in Figure 2a. At the cooling rate of 5 °C/min, the resulting LBO layer had relatively large surface roughness with a wavy texture as shown in Figure 2d. Since the morphology of the LBO-coated layer was strongly governed by the cooling methods, we carefully optimized cooling methods further.

During the second trial, we applied the following control variables: LBO layers coated twice with a slurry composition of P/A/L = 2:0:1, heating at 725 °C for 1 h. For the air-quenched samples, increasing the binder paste contents (P) by twofold led to even more severe pinoles and defects found on the coating surface, as shown in Figure 3a,b. Some of the pinholes were interconnected by severe cracks. It is believed that the pinholes were generated due to thermal decomposition of the binder in the LBO slurry composition, which will be discussed further in the following section. When pinholes are present on the coating layer, the mechanical integrity of the coating is weakened. As a result, the glass coating layer cannot withstand

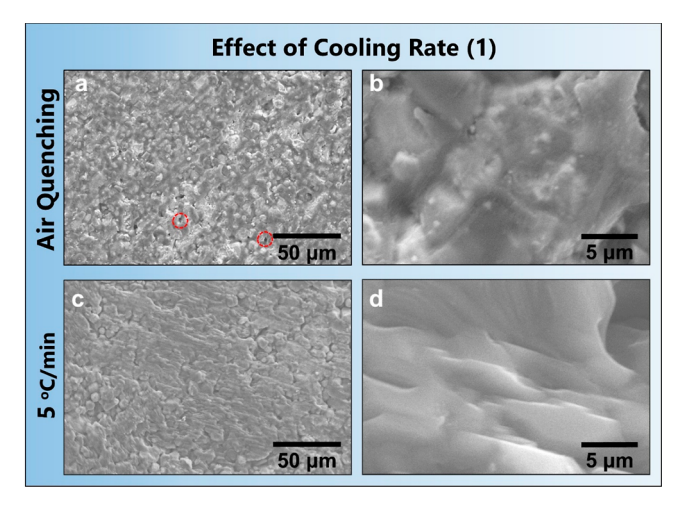


Figure 2. SEM images revealing a surface of the LBO interlayer coated onto LLZT substrate when the cooling rate was (a,b) air quenching to room temperature and (c,d) 5 °C/min. Control variables: slurry composition of P/A/L = 1:0:1, number of coated layers: 3, heating rate: 1 °C/min, and heating at 725 °C for 5 h.

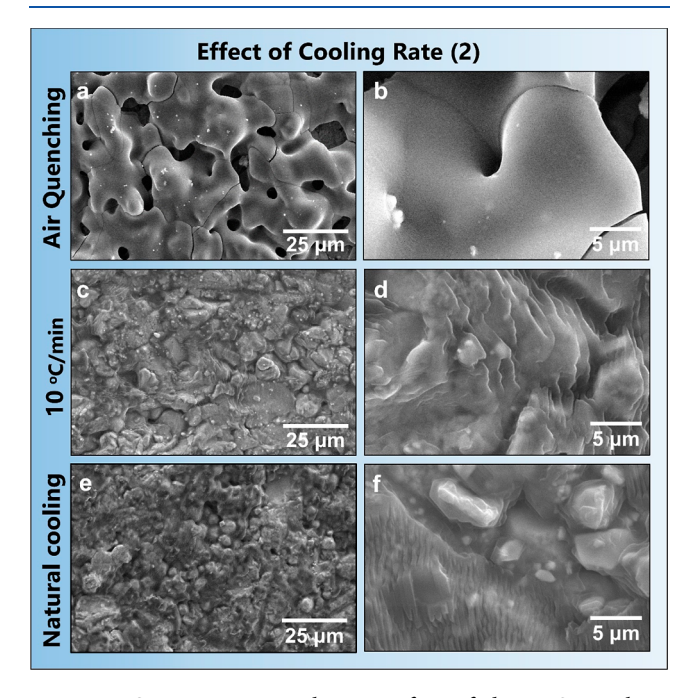


Figure 3. SEM images revealing a surface of the LBO interlayer coated onto LLZT substrate when the cooling rate was (a,b) air quenching to room temperature, (c, d) 10 °C/min, and (e,f) natural cooling. Control variables: slurry composition: P/A/L = 1:0:2, number of coated layers: 2, heating rate: 1 °C/min, and heating at 725 °C for 1 h.

the rapid thermal shrinkage during the quenching which, in turn, initiates the cracks across the surface defects (i.e., pinholes). The cracks not only degrade the mechanical integrity of the coating layer but also generate more pathways for the Li-dendrite penetration.

When the cooling rate was programmed to be 10 °C/min, pinholes and cracks no longer existed on the LBO surface, as shown in Figure 3c,d. Comparing slower 5 °C/min cooling in Figure 2b,d, a faster cooling rate created a smoother micromorphology with smaller wave dimensions. Therefore, we further increased the cooling rates to obtain a smoother LBO

surface. Because the furnace used in this work relies on passive cooling, the actual cooling rate was only ~9.2 °C/min even if 10 °C/min was programmed (see, Figure S1b). Therefore, the simplest way to maximize the cooling rate was turning off the furnace right after heat treatment (i.e., natural cooling). The temperature profile of natural cooling is also plotted in Figure S1. For the first 6 min of cooling, when the melted LBO glass interlayer solidified ($T_{\rm m}\sim 665$ °C), the natural cooling rate was well maintained to be 10 °C/min. With decreasing temperature, the cooling rates gradually decreased to 7.5 °C/ min in a range of 575-500 °C and 6.8 °C/min in a range of 500-400 °C. Such a gradual decrease in cooling rate after the solidification of the LBO glass layer could suppress the abrupt thermal expansion of the LBO layer and stress at the interface. As a result, the LBO layer had no cracks or pinholes but had a smoother surface with a very fine wavy morphology for the natural cooling. Based on these results, the natural cooling method would be recommended to prepare a conformal LBO coated layer onto the LLZT solid electrolyte.

Effect of Slurry Compositions on LBO Interlayer Coating. As mentioned earlier, slurry composition affected the quality of the LBO-coated layer under certain conditions. During the heat treatment of the LBO layer, ethyl cellulose binder in the paste thermally decomposes at around 366 °C⁴⁴ and evaporates. Therefore, too much binder content in the slurry will disrupt the uniformity of the LBO layer by leaving pinholes on the surface during the heating process. Therefore, we further optimized the LBO slurry composition by examining three different weight ratios of binder paste, alpha-terpineol, and LBO powder (P/A/L) = 1:0:1, 2:0:1,and 1:1:2. During the process, air quenching was applied as the cooling method because we were trying to force the crack generation as the indication of pinhole formation. Figure 4 showed the SEM images of the LBO layers with different slurry compositions. As discussed earlier, increasing the binder paste composition from P/A/L = 1:0:1 to 2:0:1 unwantedly increased the pinhole sizes, which accompanied crack formation along the pinholes. However, simply lowering binder paste abruptly changed the slurry viscosity that compromised the quality of the LBO layer coated via the screen-printing process. To reduce the binder content while maintaining a good slurry viscosity, we added α -terpineol solvent in the slurry and increased the LBO content. For the slurry composition of P/A/L = 1:1:2, the binder/LBO ratio was 0.5, which is lower than P/A/L = 1:0:1 with the 1.0 ratio and P/A/L = 2:0:1 with the 2.0 ratio. Figure 4c shows that the P/A/L = 1:1:2 slurry allowed us to produce the LBO layer surface free from pinholes and cracks after heat treatment. Therefore, we adopted the P/A/L = 1:1:2 slurry composition for the remaining works.

Effect of Heat Treatment Time on LBO Interlayer Coating. The effect of heat treatment time on the LBO interlayer was studied by heating the specimens at 725 °C for 0.5, 1, 2, 3, and 5 h. According to SEM images in Figure 5a, LBO powders in the slurry could not melt completely when the heat treatment time was 0.5 h (see, Figure 5a). In contrast, 5 h heat treatment led to a formation of pinholes (see, Figure 5e) that could be explained by Li evaporation from LBO. Figure 5b shows that 1 h heat treatment at 725 °C was long enough to melt all the LBO and produce a pinhole-free layer. Although heating for 2 and 3 h also created good LBO layers, they were less energy-efficient and melted LBO unwantedly

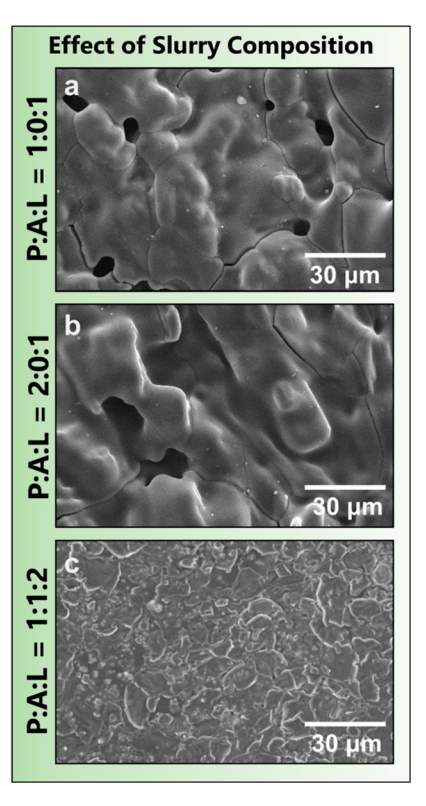


Figure 4. SEM images revealing a surface of the LBO interlayer coated onto LLZT substrate when the weight ratio of binder paste, α-terpineol, and LBO powder (P/A/L) was (a) 1:0:1, (b) 2:0:1, and (c) 1:1:2. Control variables: number of coated layers: 3, heating rate: 1 $^{\circ}$ C/min, heating at 725 $^{\circ}$ C for 5 h, and air quenching.

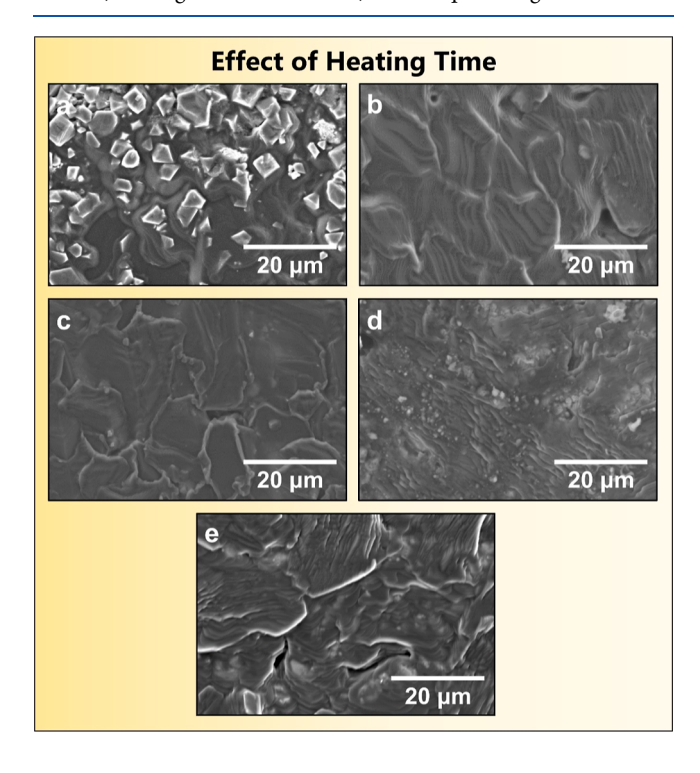


Figure 5. SEM images revealing a surface of the LBO interlayer coated onto LLZT substrate when the coated pellets were heated at 725 °C for (a) 0.5, (b) 1, (c) 2, (d) 3, and (e) 5 h. Control variables: slurry composition: P/A/L = 1:1:2, number of coated layers: 2, heating rate: 1 °C/min, heating temperature: 725 °C, and natural cooling.

with flow along the edge of the LLZT pellet during the extended period of heat treatment.

Effect of Heating Temperature on the LBO Coated Interlayer. We finally observed the effect of heating temperature on the LBO interlayer by heating the coated samples at 705, 720, 725, and 750 °C for 1 h. When the heating temperatures were 705 and 720 °C (see Figure 6a,b),

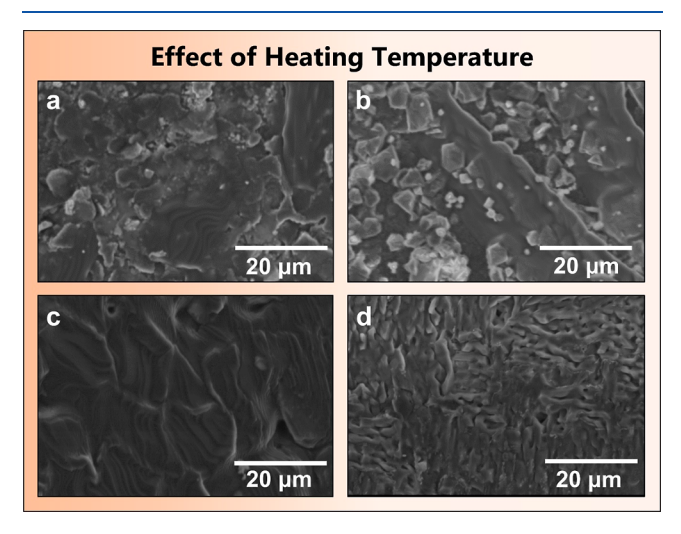


Figure 6. SEM images revealing a surface of the LBO interlayer coated onto LLZT substrate when the heat treatment temperatures were (a) 705, (b) 720, (c) 725, and (d) 750 °C for 1 h. Control variables: slurry composition: P/A/L = 1:1:2, number of coated layers: 3, heating rate: 1 °C/min, heating time: 1 h, and natural cooling.

the layer still had unmelted LBO granules. This result suggests that heating temperatures higher than 720 $^{\circ}\text{C}$ are necessary to completely melt the pristine LBO powders in the slurry under the given control variables, particularly at the short heating time (i.e., 1 h). In contrast, the LBO layer was not uniform or dense after heating at 750 $^{\circ}\text{C}$ for 1 h, as shown in Figure 6d. This could be explained by the accelerated Li evaporation at such a high temperature. When the sample was heated at 725 $^{\circ}\text{C}$ for 1 h, the coating layer was completely melted and relatively smooth without major defects, as shown in Figure 6c. Therefore, 725 $^{\circ}\text{C}$ will be an optimal heating condition under the given control variables.

Final Optimized Parameters of LBO Interlayer Coating. Following the systematic experimental design illustrated in Schematic 1, the step-by-step investigation allowed us to find each desired processing parameter. As the last step, we fabricated the LBO layer by adopting those parameters summarized in Table 2. This optimization process can be used as a useful guideline for future researchers in similar fields.

Figures 7 and S2 show that the resulting LBO coating layer was free from cracks and covering most of the pellet surface. The thickness of the coating was approximately $2-3~\mu m$. The SEM cross-section image (Figure 7c) shows that the surface roughness of LLZT substrate plays a significant role on the roughness of the LBO layer. Since the LBO layer was fabricated by the melting process, it will be reasonable to presume that its intrinsic surface roughness may be less than that of the LLZT specimen (e.g., few micrometers in this study). At the same time, the surface roughness of the LBO/LLZT solid—electrolyte specimen will not negatively impact its contact with the Li metal because Li metal was melted at 220

Table 2. List of the Examined and Finally Optimized Process Parameters for the LBO Interlayer Coating via the Screen-Printing Technique

parameters	optimized value	range of values examined
number of layers	3	2, 3
slurry composition $(P/A/L)$	1:1:2	1:0:1, 1:0:2, 1:1:2
heating rate	1 °C/min	1, 5 °C/min
temperature	725 °C	705, 720, 725, 750 °C
duration	1 h	0.5, 1, 2, 3, 5 h
cooling rate	natural cooling	1, 5, 10 $^{\circ}$ C/min, natural cooling, air quenching

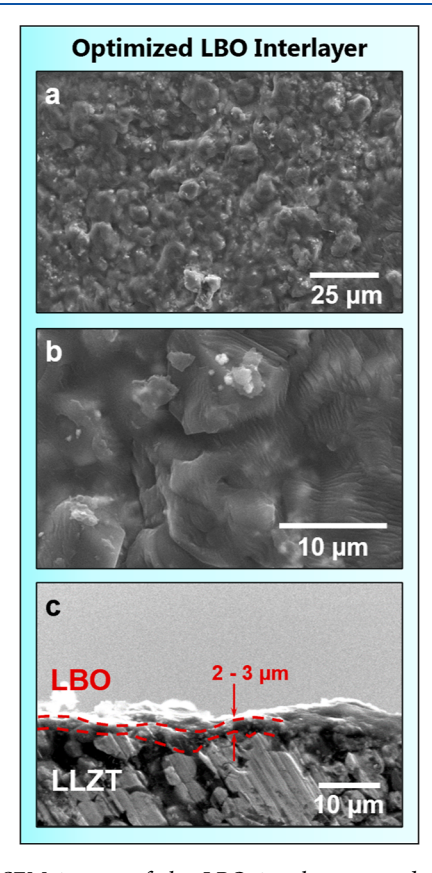


Figure 7. SEM images of the LBO interlayer coated onto LLZT substrate using the optimized values listed in Table 2: (a,b) surface of the LBO layer and (c) cross-section of the LBO-coated LLZT solid electrolyte.

°C and attached onto the solid electrolyte during a cell fabrication.

Wettability and Electrochemical Characterizations. A wettability test was performed to study the effect of the LBO interlayer on the solid—solid contact between Li-metal anode and LLZT pellets. A 0.5 mm thick Li metal was placed onto the pellets and heated at 220 °C for 5 min in an Ar-filled glovebox. After cooling to room temperature, as shown in Figure 8a, Li on the uncoated LLZT pellet could be easily peeled off using a lab tweezer. In contrast, Li strongly adhered on the LBO-coated LLZT pellet and did not peel off after the scratch test. The red dot in Figure 8b highlighted an area of Li metal where a severe scratch test was performed. The results of the wettability test showed good interfacial adhesion when the LBO coating layer was applied. Good interfacial adhesion

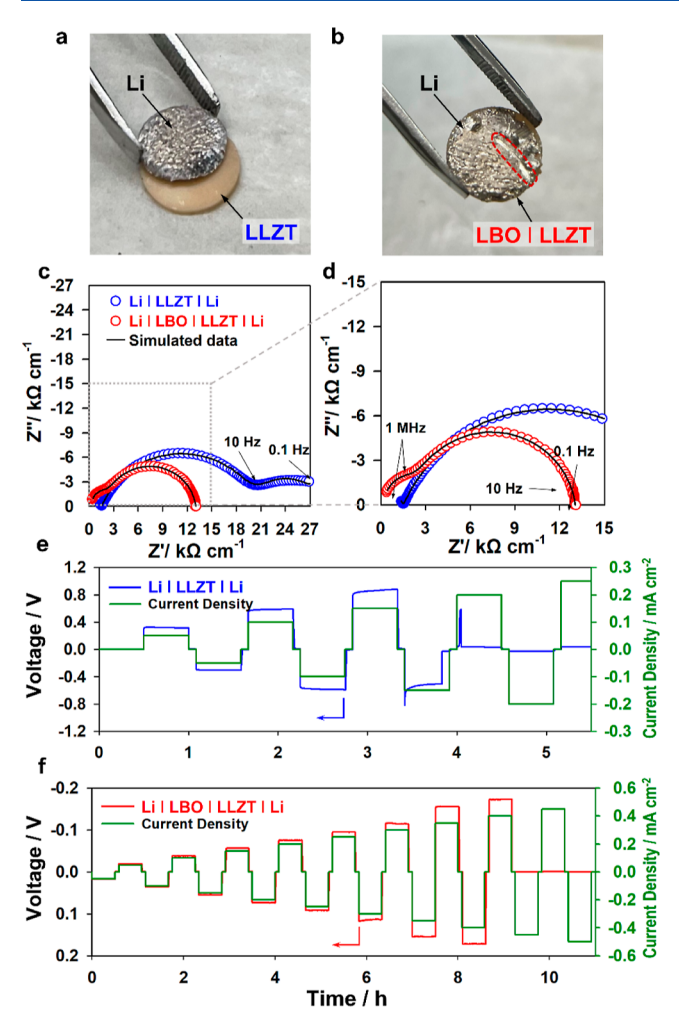


Figure 8. (a) Wettability test of the LilLLZT interface. The Li metal (silver) was easily delaminated from the LLZT pellets (light-brown disk) after applying force. (b) Wettability test of the LilLBOILLZT interface. Red dots highlight an area where the scratch testing was performed on Li metal. (c,d) Nyquist plots of LilLLZTILi and Lil LBOILLZTILi cells before cycling, which show a significant impedance reduction from the single LBO interlayer coated cell. (e,f) CCD profiles of LilLLZTILi and LilLBOILLZTILi indicating an increase in CCD from 0.15 to 0.4 mA/cm² when the LBO interlayer was applied at a single side of LLZT SE.

improves interfacial wetting and contact, which allows a uniform Li-ion current density across the surface and consequential reduction of interfacial resistance. On the other hand, poor interfacial wetting results in a limited solid—solid contacting area and local hot spots for a high and unpredictable current density that promotes dendrite growth.¹⁵

The effect of the LBO interlayer on the prevention of the Lidendrite penetration in SSLB cells was investigated by Li-metal symmetrical cells. To this end, uncoated LilLLZT|Li cells and single-side coated LilLBO|LLZT|Li cells were fabricated and examined. A double-side coated LilLBO|LLZT|LBO|Li cell could not be obtained with a good quality because the LBO layer at a bottom layer was melted and dissipated due to gravity during the heat treatment. However, this issue will not be a problem for manufacturing SSLB full cells which will have the LBO interlayer only at the anode side of LLZT electrolyte.

Figure 8c,d compares Nyquist plots of the LilLLZTILi (i.e., uncoated) and LilLBOlLLZTILi (i.e., single-side coated) cells.

For Li-symmetric cells, it was reported that the main contributors of the impedance can be assigned to the resistances of the bulk electrolyte, grain boundaries, and the Lilelectrolyte interface. 14,43,45 Therefore, we constructed three RC circuits to represent the EIS fitting curve. The bulk Li-ion conductivities of uncoated and single-side coated cells were determined to be 6.56×10^{-4} and 4.86×10^{-4} S/cm, respectively, from the high-frequency semi-circles (1 MHz). These conductivity values are comparable to the conductivity values ($\sim 10^{-4}$ S/cm) observed by previous studies. ^{22,34,43} The mid-frequency semi-circles were associated with the grain boundary conductivity, 46,47 which was determined to be 5.2 × 10^{-5} S/cm for the uncoated cell and 1.1×10^{-4} S/cm for the single-side coated cell. The interfacial conductivities were obtained in the lower-frequency ranges (i.e., 10-0.1 Hz) and determined to be 1.32×10^{-4} S/cm for the uncoated cell and 1.06×10^{-3} S/cm for the single-side coated cell. The LBO single-side coated cell had 1 order of magnitude higher interfacial conductivity due to the improved Li wetting at the Lilelectrolyte interface. Because metallic Li nucleates and deposits at the Li/SE interface, DC interfacial resistances can be calculated using Ohm's law based on the galvanostatic cycling test (Figure 8e,f),²² as shown in Figure S3. The resulting interfacial resistances were 5933 Ω cm² for the uncoated cell and 416 Ω cm² for the single-side coated cells, respectively. The latter showed approximately 14 times lower cell resistance. Both EIS and DC interfacial resistance data agree well and suggest that having the LBO layer on LLZT effectively lowers interfacial resistance.

The Li dendrite propagates under current over the critical current density (CCD), which is the largest current density allowed without an internal short circuit.48 Therefore, CCD testing has been widely adopted to examine the tolerance of cells against the Li-dendrite penetration.³³ The CCD values for uncoated and single-side coated cells were determined by galvanostatic cycling of the symmetric cells. Each galvanostatic step in the CCD was carried out for 30 min by applying 0.05 mA/cm² incremental current density, the profiles of which are plotted in Figure 8c,d. The uncoated cell experienced partial short circuits at the current density of 0.15 mA/cm² and finally shorted at 0.2 mA/cm². For the uncoated cell, current will be concentrated on limited contact areas at LilLLZT interfaces and result in non-uniform current densities across the electrode's surface. In other words, the limited contact area will experience a higher local current density than the target current density, which promotes the Li dendritic growth. 15 Therefore, the CCD value from the uncoated cell will strongly depend on the cell geometry and configurations (e.g., applying external pressure to cells). In this work, we did not apply any extra pressure on the symmetrical cell, and thus, the obtained CCD value was relatively lower than values from an earlier report.³³ On the other hand, a single-side coated cell showed a higher CCD value of 0.4 mA/cm², which is 8 times greater than that of the uncoated cell. This result can be explained by (i) more uniform current flow and (ii) suppression of Lidendrite penetration across the LilLBOILLZT interface. Furthermore, it should be noted that this result will not fully represent the capability of the LBO interlayer since the LBO interlayer was only coated on a single side of LLZT, leaving the other uncoated side to be vulnerable to the Li-dendrite growth.

Galvanostatic cycling and the resulting voltage profiles of the LilLLZT|Li (i.e., uncoated) and LilLBO|LLZT|Li (i.e., single-side coated) cells are shown Figure 9a,d, respectively. The

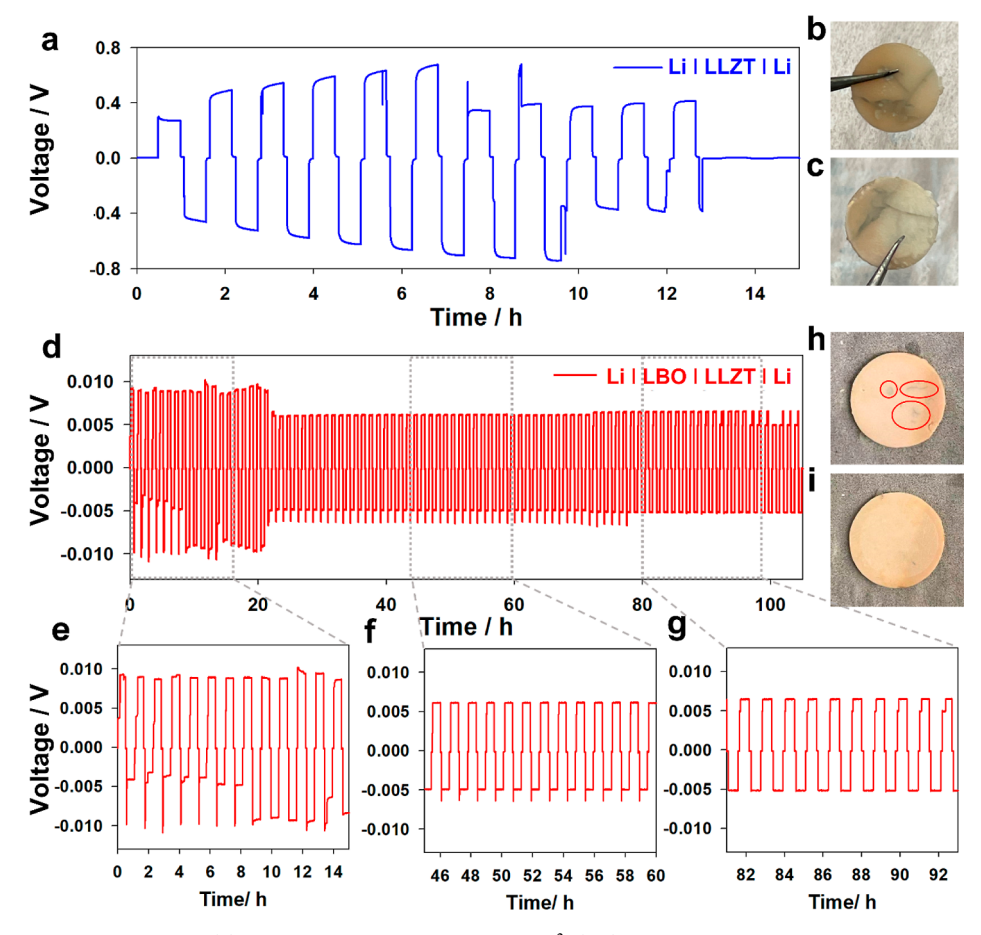


Figure 9. Galvanostatic cycling profiles of (a) LilLLZTILi cells using 0.1 mA/cm^2 . (b,c) Optical microscopy images from both sides of the uncoated cell after cycling for 13 h. (d–g) Galvanostatic cycling profiles of the LilLBOILLZTILi cell using 0.1 mA/cm^2 . Optical microscopy image of (h) uncoated side and (i) coated side of the cell after 93 cycles (105 h). Traces of defects are circled in red.

uncoated cell showed 6 h of steady cycling performance until the sudden voltage drops after the 7th cycle and eventual cell shorting at the 11th cycle (see, Figure 9a). During the first 6 cycles, the cell voltage range kept increasing from 0.3 to 0.7 V during cycling, which is indicative of cell resistance growth. This result can be explained by a poor Li-metal wetting in contact with LLZT SE during repeated plating/stripping cycles. Li dendrites might grow at the beginning of the cycling, and partial Li-dendrite penetration into LLZT SE led to a current leak through the electrolyte and cell voltage drop at the 7th cycle. At the 11th cycle, Li-dendrite penetration resulted in the cell shorting. The failed uncoated cell was taken out from the Swagelok cell and Li metal was able to be peeled off easily from the LLZT pellet, which again indicated their weak adhesion due to the poor wetting. Figure 9b,c shows dark stripe of the Li dendrite across the LLZT SE, which was reported in the literature.⁴⁹ The Li dendrites inside LLZT not only penetrated the pellet but also generated micro-crack-like features across the pellets in a short period of time. 50,5

In contrast, the single-side coated LilLBOILLZTILi cell was able to cycle for 105 h without an internal short circuit as shown in Figure 9d. During the first 20 cycles (see, Figure 9e), the cell had some voltage fluctuation, which may be associated with solid electrolyte interface (SEI) growth at LilLLZT (for the uncoated side of the cell) and LilLBO (for the coated side of the cell). After 20 cycles, the cell delivered a stable overpotential value of ~6 mV at a current density of 0.1 mA/cm², which is close to the reported values in the literature. For

example, Nagao et al. 1 reported that the Li/LBO-Li $_2$ SO $_4$ (glass-SE)/Li symmetrical cell delivered ~30 mV overpotential at a current density of 0.25 mA/cm 2 . It is also notable that the voltage scales of the single-side coated cell were always asymmetric: higher ΔV during charging and lower ΔV during discharging. This can be explained by considering the cell configuration: positivelLilLBO|LLZT|Lilnegative. During charging, the Li plating occurs at the bare LilLZT interface and Li stripping occurs at the LilLBO|LLZT interface. In contrast, the Li plating occurs at the LilLBO|LLZT interfaces during discharging, which maintains better Li wetting and thus lower interfacial impedance during the process.

Figure 9f,g shows that the Li plating and stripping voltages become more stable after 20 h operation (~20 cycles), indicating the completion of the Li SEI layer and more stable Li transport across the interfaces. The cell was cycled for ~ 105 h (93 cycles) with stable voltage profiles without any signals of cell failure. After the cycling, the LilLBOILLZTILi cell was open and the electrolyte pellet was collected for a visual inspection. Unlike the uncoated cell, Li metal had strong adhesion onto the LBO layer and was difficult to be removed. Therefore, the Li metal was carefully sanded out using sandpaper in an Ar glovebox. The resulting LLZT pellet showed little spots with discoloration, which might indicate a trace amount of Li-metal deposition inside LLZT grain boundaries.⁵² On the other hand, the uncoated side (Figure 9h) showed several dark spots (circled in red), which indicated the possible local Li-dendrite penetration. However, the singleside coated LLZT pellet did not show any notable long-range defects compared with the uncoated LLZT pellet. Even the local Li-dendrite penetration across the LLZT pellet could be blocked by the LBO layer, as evidenced by stable cycling of the LilLBO|LLZT|Li cell.

CONCLUSIONS

In this work, systematic design of experiments revealed optimized synthesis parameters to obtain a thin and uniform LBO interlayer in between the solid electrolyte (LLZT) and Li anode. Further, we demonstrated positive roles of the LBO interlayer to enhance the Li-metal wetting and prevent the Lidendrite penetration during SSLB cycling. To optimize the synthesis parameters, we performed step-by-step experiments that could examine the effects of heating rates, cooling rates, LBO slurry compositions, heating temperatures, and heating times. Thorough investigation allowed to obtain a uniform LBO-coated interlayer with \sim 5 μ m thickness onto LLZT pellets by finding each desired processing parameter: (i) LBO slurry with a composition of P/A/L = 1:1:2, (ii) a heating rate of 1 °C/min, (iii) heating at 725 °C for 1 h, and (iv) natural cooling. The LBO interlayer was able to improve interfacial wetting of the Li-metal anode as evidenced by the increase in interfacial conductivity from 1.32×10^{-4} to 1.06×10^{-3} S/cm. In addition, the LilLBO|LLZT|Li symmetrical cell, having the LBO layer only at one side, increased the CCD value from 0.15 mA/cm² (from LBO-free cell) to 0.4 mA/cm². Although the LBO-free LilLLZTILi cell experienced the internal short circuit after 13 h operation due to the Li-dendrite penetration, the Lil LBO|LLZT|Li cell showed stable performance for more than 100 h under the current density of 0.1 mA/cm². After 105 h cycling test, the optical microscopy images of LLZT recovered from the LilLBOILLZTILi cell showed no sign of severe defects, confirming the positive role of the LBO interlayer in preventing the Li-dendrite penetration.

ASSOCIATED CONTENT

Supporting Information

The Supporting Information is available free of charge at https://pubs.acs.org/doi/10.1021/acsaem.2c01606.

Temperature profile of the natural cooling process, SEM cross-section images, and Ohmic resistance of symmetrical cells during CCD testing (PDF)

AUTHOR INFORMATION

Corresponding Authors

Jay R. Sayre — Department of Materials Science and Engineering, The Ohio State University, Columbus, Ohio 43210, United States; Email: sayre.17@osu.edu

Jung-Hyun Kim — Center for Automotive Research,
Department of Mechanical and Aerospace Engineering, The
Ohio State University, Columbus, Ohio 43210, United
States; ⑤ orcid.org/0000-0002-4598-4686;
Email: kim.6776@osu.edu

Authors

Zhenghuan Tang — Center for Automotive Research,
Department of Mechanical and Aerospace Engineering, The
Ohio State University, Columbus, Ohio 43210, United States
Junbin Choi — Center for Automotive Research, Department of
Mechanical and Aerospace Engineering, The Ohio State
University, Columbus, Ohio 43210, United States

- Jose L. Lorie Lopez Department of Chemistry and Biochemistry, The Ohio State University, Columbus, Ohio 43210, United States; Oorcid.org/0000-0002-1365-3815
- Anne C. Co Department of Chemistry and Biochemistry, The Ohio State University, Columbus, Ohio 43210, United States; orcid.org/0000-0002-3546-1582
- Christopher J. Brooks North American Auto Development Center, Honda Development and Manufacturing of America, LLC, Raymond, Ohio 43067, United States; ⊚ orcid.org/ 0000-0003-1445-2035

Complete contact information is available at: https://pubs.acs.org/10.1021/acsaem.2c01606

Notes

The authors declare no competing financial interest.

ACKNOWLEDGMENTS

This work was supported by Honda Development & Manufacturing of America, LLC.

REFERENCES

- (1) Lim, H.-D.; Park, J.-H.; Shin, H.-J.; Jeong, J.; Kim, J. T.; Nam, K.-W.; Jung, H.-G.; Chung, K. Y. A Review of Challenges and Issues Concerning Interfaces for All-Solid-State Batteries. *Energy Storage Mater.* **2020**, 25, 224–250.
- (2) Thangadurai, V.; Narayanan, S.; Pinzaru, D. Garnet-Type Solid-State Fast Li Ion Conductors for Li Batteries: Critical Review. *Chem. Soc. Rev.* **2014**, *43*, 4714–4727.
- (3) Salami, T. J.; Imanieh, S. H.; Lawrence, J. G.; Martin, I. R. Amorphous Glass-Perovskite Composite as Solid Electrolyte for Lithium-Ion Battery. *Mater. Lett.* **2019**, 254, 294–296.
- (4) Jolley, A. G.; Cohn, G.; Hitz, G. T.; Wachsman, E. D. Improving the Ionic Conductivity of NASICON through Aliovalent Cation Substitution of Na3Zr2Si2PO12. *Ionics* **2015**, *21*, 3031–3038.
- (5) Wang, C.; Bai, G.; Yang, Y.; Liu, X.; Shao, H. Dendrite-Free All-Solid-State Lithium Batteries with Lithium Phosphorous Oxynitride-Modified Lithium Metal Anode and Composite Solid Electrolytes. *Nano Res.* **2019**, *12*, 217–223.
- (6) Lü, X.; Wu, G.; Howard, J. W.; Chen, A.; Zhao, Y.; Daemen, L. L.; Jia, Q. Li-rich anti-perovskite Li3OCl films with enhanced ionic conductivity. *Chem. Commun.* **2014**, *50*, 11520–11522.
- (7) Sastre, J.; Chen, X.; Aribia, A.; Tiwari, A. N.; Romanyuk, Y. E. Fast Charge Transfer across the Li7La3Zr2O12 Solid Electrolyte/LiCoO2 Cathode Interface Enabled by an Interphase-Engineered All-Thin-Film Architecture. ACS Appl. Mater. Interfaces 2020, 12, 36196—36207.
- (8) Zhao, N.; Khokhar, W.; Bi, Z.; Shi, C.; Guo, X.; Fan, L.-Z.; Nan, C.-W. Solid Garnet Batteries. *Joule* **2019**, *3*, 1190–1199.
- (9) Thangadurai, V.; Pinzaru, D.; Narayanan, S.; Baral, A. K. Fast Solid-State Li Ion Conducting Garnet-Type Structure Metal Oxides for Energy Storage. *J. Phys. Chem. Lett.* **2015**, *6*, 292–299.
- (10) El Shinawi, H.; Janek, J. Stabilization of cubic lithium-stuffed garnets of the type "Li7La3Zr2O12" by addition of gallium. *J. Power Sources* **2013**, 225, 13–19.
- (11) Huang, M.; Dumon, A.; Nan, C.-W. Effect of Si, In and Ge Doping on High Ionic Conductivity of Li7La3Zr2O12. *Electrochem. Commun.* **2012**, *21*, 62–64.
- (12) Allen, J. L.; Wolfenstine, J.; Rangasamy, E.; Sakamoto, J. Effect of Substitution (Ta, Al, Ga) on the Conductivity of Li7La3Zr2O12. *J. Power Sources* **2012**, *206*, 315–319.
- (13) Li, Y.; Han, J.-T.; Wang, C.-A.; Xie, H.; Goodenough, J. B. Optimizing Li+ Conductivity in a Garnet Framework. *J. Mater. Chem.* **2012**, 22, 15357.
- (14) Lou, J.; Wang, G.; Xia, Y.; Liang, C.; Huang, H.; Gan, Y.; Tao, X.; Zhang, J.; Zhang, W. Achieving Efficient and Stable Interface between Metallic Lithium and Garnet-Type Solid Electrolyte through

- a Thin Indium Tin Oxide Interlayer. J. Power Sources 2020, 448, 227440.
- (15) Liu, H.; Cheng, X.-B.; Huang, J.-Q.; Yuan, H.; Lu, Y.; Yan, C.; Zhu, G.-L.; Xu, R.; Zhao, C.-Z.; Hou, L.-P.; He, C.; Kaskel, S.; Zhang, Q. Controlling Dendrite Growth in Solid-State Electrolytes. *ACS Energy Lett.* **2020**, *5*, 833–843.
- (16) Shen, K.; Wang, Y.; Zhang, J.; Zong, Y.; Li, G.; Zhao, C.; Chen, H. Revealing the effect of grain boundary segregation on Li ion transport in polycrystalline anti-perovskite Li3ClO: a phase field study. *Phys. Chem. Chem. Phys.* **2020**, 22, 3030–3036.
- (17) Ji, X.; Hou, S.; Wang, P.; He, X.; Piao, N.; Chen, J.; Fan, X.; Wang, C. Solid-State Electrolyte Design for Lithium Dendrite Suppression. *Adv. Mater.* **2020**, 32, 2002741.
- (18) Yu, S.; Siegel, D. J. Grain Boundary Softening: A Potential Mechanism for Lithium Metal Penetration through Stiff Solid Electrolytes. ACS Appl. Mater. Interfaces 2018, 10, 38151–38158.
- (19) Cheng, X.-B.; Zhao, C.-Z.; Yao, Y.-X.; Liu, H.; Zhang, Q. Recent Advances in Energy Chemistry between Solid-State Electrolyte and Safe Lithium-Metal Anodes. *Chem* **2019**, *5*, 74–96.
- (20) Li, Y.; Chen, X.; Dolocan, A.; Cui, Z.; Xin, S.; Xue, L.; Xu, H.; Park, K.; Goodenough, J. B. Garnet Electrolyte with an Ultralow Interfacial Resistance for Li-Metal Batteries. *J. Am. Chem. Soc.* **2018**, 140, 6448–6455.
- (21) Xu, B.; Li, W.; Duan, H.; Wang, H.; Guo, Y.; Li, H.; Liu, H. Li 3 PO 4 -Added Garnet-Type Li 6.5 La 3 Zr 1.5 Ta 0.5 O 12 for Li-Dendrite Suppression. *J. Power Sources* **2017**, 354, 68–73.
- (22) Rosero-Navarro, N. C.; Kajiura, R.; Jalem, R.; Tateyama, Y.; Miura, A.; Tadanaga, K. Significant Reduction in the Interfacial Resistance of Garnet-Type Solid Electrolyte and Lithium Metal by a Thick Amorphous Lithium Silicate Layer. ACS Appl. Energy Mater. 2020, 3, 5533–5541.
- (23) Tian, Y.; Ding, F.; Zhong, H.; Liu, C.; He, Y.-B.; Liu, J.; Liu, X.; Xu, Q. Li6.75La3Zr1.75Ta0.25O12@amorphous Li3OCl Composite Electrolyte for Solid State Lithium-Metal Batteries. *Energy Storage Mater.* **2018**, *14*, 49–57.
- (24) Solid Electrolytes for Advanced Applications: Garnets and Competitors; Murugan, R., Weppner, W., Eds.; Springer International Publishing: Cham, 2019.
- (25) Kim, K. Y.; Park, S. B. Preparation and Property Control of Nano-Sized Indium Tin Oxide Particle. *Mater. Chem. Phys.* **2004**, *86*, 210–221.
- (26) Richet, P.; Mysen, B. O.; Andrault, D. Melting and Premelting of Silicates: Raman Spectroscopy and X-Ray Diffraction of Li2SiO3 and Na2SiO3. *Phys. Chem. Miner.* **1996**, 23, 157.
- (27) Han, N. T.; Dien, V. K.; Lin, M.-F. Excitonic Effects in the Optical Spectra of Lithium Metasilicate (Li2SiO3). 2020, arXiv:2010.11621.
- (28) Zhao, G.; Suzuki, K.; Seki, T.; Sun, X.; Hirayama, M.; Kanno, R. High lithium ionic conductivity of γ -Li3PO4-type solid electrolytes in Li4GeO4–Li4SiO4-Li3VO4 quasi-ternary system. *J. Solid State Chem.* **2020**, 292, 121651.
- (29) Tadanaga, K.; Takano, R.; Ichinose, T.; Mori, S.; Hayashi, A.; Tatsumisago, M. Low temperature synthesis of highly ion conductive Li7La3Zr2O12-Li3BO3 composites. *Electrochem. Commun.* **2013**, 33, 51–54.
- (30) Nagao, K.; Nose, M.; Kato, A.; Sakuda, A.; Hayashi, A.; Tatsumisago, M. Preparation and Characterization of Glass Solid Electrolytes in the Pseudoternary System Li 3 BO 3 -Li 2 SO 4 -Li 2 CO 3. *Solid State Ionics* **2017**, *308*, 68–76.
- (31) Nagao, K.; Suyama, M.; Kato, A.; Hotehama, C.; Deguchi, M.; Sakuda, A.; Hayashi, A.; Tatsumisago, M. Highly Stable Li/Li3BO3-Li2SO4 Interface and Application to Bulk-Type All-Solid-State Lithium Metal Batteries. ACS Appl. Energy Mater. 2019, 2, 3042—3048.
- (32) Ren, Y.; Shen, Y.; Lin, Y.; Nan, C.-W. Direct Observation of Lithium Dendrites inside Garnet-Type Lithium-Ion Solid Electrolyte. *Electrochem. Commun.* **2015**, *57*, 27–30.
- (33) Hosokawa, H.; Takeda, A.; Inada, R.; Sakurai, Y. Tolerance for Li Dendrite Penetration in Ta-Doped Li7La3Zr2O12 Solid Electro-

- lytes Sintered with Li2.3C0.7B0.3O3 Additive. Mater. Lett. 2020, 279, 128481.
- (34) Choi, J.; Kim, J.-H. Composition Structure Property relationship of Li2.3C0.7B0.3O3 Li6.4La3Zr1.4Ta0.6O12 for composite cathodes in all solid-state batteries. *Solid State Ionics* **2022**, *378*, 115900.
- (35) Chen, G.-W.; Gong, Z. L. Study on Li3BO3 Interface Modification of Garnet Solid Electrolyte. *J. Electrochem.* **2020**, *27*, 76.
- (36) Xia, W.; Xu, B.; Duan, H.; Tang, X.; Guo, Y.; Kang, H.; Li, H.; Liu, H. Reaction Mechanisms of Lithium Garnet Pellets in Ambient Air: The Effect of Humidity and CO2. *J. Am. Ceram. Soc.* **2017**, *100*, 2832–2839.
- (37) Sharafi, A.; Yu, S.; Naguib, M.; Lee, M.; Ma, C.; Meyer, H. M.; Nanda, J.; Chi, M.; Siegel, D. J.; Sakamoto, J. Impact of air exposure and surface chemistry on Li-Li7La3Zr2O12 interfacial resistance. *J. Mater. Chem. A* **2017**, *5*, 13475–13487.
- (38) Tian, H.-K.; Xu, B.; Qi, Y. Computational Study of Lithium Nucleation Tendency in Li7La3Zr2O12 (LLZO) and Rational Design of Interlayer Materials to Prevent Lithium Dendrites. *J. Power Sources* **2018**, 392, 79–86.
- (39) Senevirathne, K.; Day, C. S.; Gross, M. D.; Lachgar, A.; Holzwarth, N. A. W. A New Crystalline LiPON Electrolyte: Synthesis, Properties, and Electronic Structure. *Solid State Ionics* **2013**, 233, 95–101
- (40) Perentzis, G.; Horopanitis, E. E.; Pavlidou, E.; Papadimitriou, L. Thermally Activated Ionic Conduction in LiNbO3 Electrolyte Thin Films. *Mater. Sci. Eng., B* **2004**, *108*, 174–178.
- (41) Homma, K.; Liu, Y.; Sumita, M.; Tamura, R.; Fushimi, N.; Iwata, J.; Tsuda, K.; Kaneta, C. Optimization of a Heterogeneous Ternary Li3PO4-Li3BO3-Li2SO4 Mixture for Li-Ion Conductivity by Machine Learning. *J. Phys. Chem. C* **2020**, *124*, 12865–12870.
- (42) Il'ina, E. A.; Pershina, S. V.; Antonov, B. D.; Pankratov, A. A.; Vovkotrub, E. G. The Influence of the Glass Additive Li2O-B2O3-SiO2 on the Phase Composition, Conductivity, and Microstructure of the Li7La3Zr2O12. *J. Alloys Compd.* **2018**, 765, 841–847.
- (43) Paksi Raganata, G.; Kartini, E.; Jodi, H.; Wahyudianingsih; Sudjatno, A.; Nicolas Gunawidjaja, P. Synthesize & Characterization of Li3PO4(0.5)LiI(0.25)LiCl(0,25) Solid Electrolyte for Lithium Ion Battery. *IOP Conf. Ser.: Mater. Sci. Eng.* **2020**, 924, 012037.
- (44) Trivedi, M. K.; Branton, A.; Trivedi, D.; Nayak, G.; Mishra, R. K.; Jana, S. Characterization of Physicochemical and Thermal Properties of Biofield Treated Ethyl Cellulose and Methyl Cellulose. *Int. J. Biomed. Mater. Res.* **2015**, *3*, 83.
- (45) Cheng, L.; Wu, C. H.; Jarry, A.; Chen, W.; Ye, Y.; Zhu, J.; Kostecki, R.; Persson, K.; Guo, J.; Salmeron, M.; Chen, G.; Doeff, M. Interrelationships among Grain Size, Surface Composition, Air Stability, and Interfacial Resistance of Al-Substituted Li7La3Zr2O12 Solid Electrolytes. ACS Appl. Mater. Interfaces 2015, 7, 17649–17655.
- (46) Huang, X.; Xiu, T.; Badding, M. E.; Wen, Z. Two-Step Sintering Strategy to Prepare Dense Li-Garnet Electrolyte Ceramics with High Li+ Conductivity. *Ceram. Int.* **2018**, *44*, 5660–5667.
- (47) Huang, Z.; Liu, K.; Chen, L.; Lu, Y.; Li, Y.; Wang, C.-A. Sintering behavior of garnet-type Li6.4 La3 Zr1.4 Ta0.6 O12 in Li2 CO3 atmosphere and its electrochemical property. *Int. J. Appl. Ceram. Technol.* **2017**, *14*, 921–927.
- (48) Cao, D.; Sun, X.; Li, Q.; Natan, A.; Xiang, P.; Zhu, H. Lithium Dendrite in All-Solid-State Batteries: Growth Mechanisms, Suppression Strategies, and Characterizations. *Matter* **2020**, *3*, 57–94.
- (49) Aguesse, F.; Manalastas, W.; Buannic, L.; Lopez del Amo, J. M.; Singh, G.; Llordés, A.; Kilner, J. Investigating the Dendritic Growth during Full Cell Cycling of Garnet Electrolyte in Direct Contact with Li Metal. *ACS Appl. Mater. Interfaces* **2017**, *9*, 3808–3816.
- (50) Sharafi, A.; Meyer, H. M.; Nanda, J.; Wolfenstine, J.; Sakamoto, J. Characterizing the Li-Li7La3Zr2O12 interface stability and kinetics as a function of temperature and current density. *J. Power Sources* **2016**, 302, 135–139.
- (51) Cheng, E. J.; Sharafi, A.; Sakamoto, J. Intergranular Li Metal Propagation through Polycrystalline Li6.25Al0.25La3Zr2O12 Ceramic Electrolyte. *Electrochim. Acta* **2017**, 223, 85–91.

(52) Rajendran, S.; Thangavel, N. K.; Mahankali, K.; Arava, L. M. R. Toward Moisture-Stable and Dendrite-Free Garnet-Type Solid-State Electrolytes. ACS Appl. Energy Mater. 2020, 3, 6775-6784.

Recommended by ACS

Free-Standing and Flexible Garnet-PVDF Ceramic Polymer **Electrolyte Membranes for Solid-State Batteries**

Sreejith O. V., Murugan Ramaswamy, et al.

JANUARY 24, 2023 **ENERGY & FUELS**

READ

Water-Based Fabrication of a Li|Li₇La₃Zr₂O₁₂|LiFePO₄ Solid-State Battery-Toward Green Battery Production

Ruijie Ye, Egbert Figgemeier, et al.

JUNE 01, 2022

ACS SUSTAINABLE CHEMISTRY & ENGINEERING

READ 🗹

A High-Filled Li₇La₃Zr₂O₁₂/Polypropylene Oxide Composite Solid Electrolyte with Improved Lithium-Ion Transport and Safety Performances for High-Voltage Li B...

Jie Li, Mao-xiang Jing, et al.

AUGUST 15, 2022

ACS APPLIED ENERGY MATERIALS

READ 🗹

$Ultrathin\ Li_{6.75}La_{3}Zr_{1.75}Ta_{0.25}O_{12}\text{-}Based\ Composite\ Solid$ **Electrolytes Laminated on Anode and Cathode Surfaces for Anode-free Lithium Metal Batteries**

Tilahun Awoke Zegeye, Bing Joe Hwang, et al.

NOVEMBER 13, 2020

ACS APPLIED ENERGY MATERIALS

READ

Get More Suggestions >